PAPER

Check for updates

Performance degradation study of NiCo$_2$O$_4$-based asymmetric supercapacitors

Guanlun Guo, [ID] *[a] Yilong Mei,[a] Xu Chen,[a] Jun Liu[b] and Wentao Liu[c]

The performance of NiCo$_2$O$_4$//GO asymmetric supercapacitors was found to decline after many tests. It was found that the performance of the GO electrode was almost unchanged, while the performance of the NiCo$_2$O$_4$ electrode declined rapidly. Therefore, porous spherical NiCo$_2$O$_4$ nanoparticles were synthesized *via* a simple hydrothermal method. A NiCo$_2$O$_4$//GO asymmetric supercapacitor was made, which can be charged and discharged 3000 times in the current density of 10 A g^{-1}. The surface morphology, crystal structure and elemental composition were characterized by X-ray diffraction analysis, scanning electron microscopy and X-ray photoelectron spectroscopy. By comparing the surface morphology, crystal structure and elemental composition of the NiCo$_2$O$_4$ electrode before and after the cycle, it was found that the performance of NiCo$_2$O$_4$ electrode declines rapidly after the cycle due to the formation of new substances and the destruction of the crystal structure of NiCo$_2$O$_4$ electrode. Therefore, maintaining the stability of the crystal structure of the electrode material is an important means to ensure the stability of the performance of the supercapacitor. It provides a meaningful strategy for studying the degradation of supercapacitor electrode materials.

1. Introduction

The supercapacitor is a new type of energy storage equipment with electrochemical performance between lithium-ion batteries and traditional capacitors. It has the characteristics of high power density, high charge–discharge speed, wide operating temperature limit, excellent cycle stability and safety, *etc.* It is used as an alternative or supplement to batteries on the occasions of high power output or fast energy collection, such as electric vehicle composite energy storage systems, rail transit, wind power and photovoltaic power generation. The high power density of supercapacitors is mainly due to the fact that the energy storage process of supercapacitors takes place on the surface or near the surface of electrode materials, and the charge storage and release are very quickly. Unlike lithium-ion batteries, during the energy storage process, electrolyte ions will go deep into the lattice and cause crystal phase transition. The charge storage and release process is limited by the diffusion of ions in the lattice and the process is slow. The fast energy storage process also endows the supercapacitor with high charge–discharge efficiency and long cycle life.[1–5]

The electrode material is the core component of the supercapacitor, which largely determines the energy storage mechanism and electrochemical performance of the supercapacitor. In recent years, pseudocapacitors have been widely studied because of their higher energy density compared with double-layer capacitors.[6–11] The main application value of supercapacitors is their high power characteristics, but they also need a high enough energy density to store more energy for output. Transition metal oxides are one of the main electrode materials for pseudocapacitors, which can be stored by reversible redox reactions on or near the surface of active materials.[12]

As a kind of spinel oxide, NiCo$_2$O$_4$ has great potential as a pseudocapacitor electrode material. This strong crystal structure makes the redox reaction process of Ni^{2+}/Ni^{3+}, Co^{2+}/Co^{3+} and Co^{3+}/Co^{4+} highly reversible, which keeps the material stable and improves the cycle stability. Sun *et al.*[13] prepared nanosheet self-assembled spinel NiMn$_2$O$_4$ microspheres grown directly on three-dimensional nickel foam through a simple microwave-assisted hydrothermal process. Taking 6 M KOH as electrolyte, the specific capacitance of 768.9 F g^{-1} at 1 A g^{-1} current density is shown. Bao *et al.*[14] directly synthesized mesoporous ZnCo$_2$O$_4$ nanosheet arrays with strong adhesion on highly conductive nickel foam by hydrothermal calcination, and then directly used them as integrated electrodes. Using 2 M KOH as electrolyte, the specific capacitance of 2468 F g^{-1} was obtained at 5 A g^{-1} current density. At the current density of 30 A g^{-1}, the capacitor retention rate is 96.3% after 1500 cycles.

To study the reason of performance decline of NiCo$_2$O$_4$//GO asymmetric supercapacitor. In this paper, NiCo$_2$O$_4$ nanoparticles were synthesized by hydrothermal method. The prepared NiCo$_2$O$_4$ nanoparticles were used as the electrode

[a]Hubei Key Laboratory of Advanced Technology for Automotive Components, Hubei Research Center for New Energy & Intelligent Connected Vehicle, University of Technology, Wuhan 430070, China. E-mail: glguo@whut.edu.cn

[b]Wuhan Huaxia University of Technology, Wuhan 430223, China

[c]Shandong Academy of Pharmaceutical Science, Jinan 250101, PR China

active material, and nickel foam was used as the collecting system to form the electrode sheet. In the three-electrode system, platinum wire was used as the counter electrode, Hg/HgO electrode was the reference electrode, and 6 M KOH solution was used as the electrolyte to form a half cell. The electrochemical performance was measured by cyclic voltammetry test, constant current charge–discharge test, electrochemical impedance test and cyclic stability test. $NiCo_2O_4$//GO asymmetric supercapacitors were fabricated with $NiCo_2O_4$ cathode electrode and GO anode electrode, which were charged and discharged for 3000 times in a current density of 10 A g^{-1}. The degradation of electrode performance after 3000 cycles is sufficient to study the mechanism of the degradation. For the recycled material, ethanol is used as a dispersant to ultrasonic treatment the electrode sheet for 10 min to obtain recycled particles, which can eliminate the influence of binder. The surface morphology, crystal structure and elemental composition of the electrode active material recovered from the asymmetric supercapacitor after cycling were characterized in detail, and the decay mechanism was studied by comparing with that of the raw material.

2. Experimental section

2.1 Preparation and characterization of $NiCo_2O_4$ powders

$NiCo_2O_4$ nanoparticles were prepared by hydrothermal method, and urea ($CO(NH_2)_2$) was used as the reducing and precipitating agent. Firstly, $Ni(NO_3)_2$–$6H_2O$, $Co(NO_3)_2$–$6H_2O$ and CH_4N_2O were weighed according to 1 : 2 : 6, and they were dissolved and evenly mixed in 70 mL of 1 : 1 mixed solvent of deionized water and ethanol using a magnetic stirrer. Then the reactant mixture was poured into a PTFE-lined autoclave, and the reactor was put into an electric blast drying oven for hydrothermal reaction with a setting temperature of 120 °C for 8 h. Then the precipitate was obtained by centrifugation using a centrifuge, washed three times each with ethanol and deionized water cross, and then the precipitate was dried using a vacuum drying oven with a setting temperature of 80 °C for 8 h. After that, the dried powdered precipitate was transferred to a crucible and calcined at a medium temperature of 300 °C for 3 h. Finally, the calcined powder was ground and dispersed in a mortar to obtain black powdered $NiCo_2O_4$ nanoparticles.

2.2 Electrochemical measurements

Electrochemical measurements were performed on $NiCo_2O_4$ electrodes and $NiCo_2O_4$-based asymmetric supercapacitor in a three-electrode system and a two-electrode system, respectively, to investigate the factors and mechanisms of degradation. Using treated nickel foam as the substrate, polyvinylidene fluoride as the binder and acetylene black as the conductive agent, the active material, binder and conductive agent are weighed in the mass ratio of 8 : 1 : 1, and the three are ground and mixed evenly using a mortar and pestle, and an appropriate amount of 1-methyl-2-pyrrolidone is added, and the grinding is continued to dissolve polyvinylidene fluoride completely. The active material slurry is evenly coated on the surface of the dry fluid collection. After that,

it is dried by vacuum drying oven and finally the mixture is pasted on the nickel foam by pressing device to form the working electrode. In the three-electrode system, the electrode for preparing $NiCo_2O_4$ is used as the working electrode, the platinum wire is used as the counter electrode, and the Hg/HgO electrode is used as the reference electrode. In the two-electrode system, $NiCo_2O_4$ electrode and GO electrode were prepared by the same preparation method as positive and negative electrode sheets, and 6 M KOH solution was used as electrolyte to form a full cell for electrochemical performance testing. Three electrochemical tests namely cyclic voltammetry (CV) test, galvanostatic charge–discharge (GCD) tests and cyclic charge–discharge test, were carried out utilizing an electrochemical workstation CS150 (Corrtest Co. Ltd, Wuhan). The specific capacitance was calculated from GCD curves according to the following equation.

$$C = \frac{I\Delta t}{m\Delta V} \tag{1}$$

where I is the discharge current, Δt is the discharge time, m is the mass of the active material and ΔV is the voltage scan range.

3. Results and discussion

3.1 Phase composition, microstructure and surface chemistry

Fig. 1(a) shows the XRD patterns of prepared $NiCo_2O_4$ samples. Comparison with XRD standard card PDF#73-1702 shows that there are distinct diffraction peaks at 2θ values of 18.9°, 31.2°, 36.7°, 38.4°, 44.6°, 55.4°, 59.1°, 64.9°, 77.0°, corresponding to (1 1 1), (2 2 0), (3 1 1), (2 2 2), (4 0 0), (4 2 2), (5 1 1), (4 4 0), and (5 3 3) crystal surfaces of $NiCo_2O_4$. No other obvious non-$NiCo_2O_4$ diffraction peaks were observed, and the unique crystal phase of $NiCo_2O_4$ was observed, indicating that the prepared material is high purity $NiCo_2O_4$.

According to the standard card, the crystal structure of the prepared $NiCo_2O_4$ can be determined as a cubic crystal system with $Fd\bar{3}m$ space group. The nanoparticles consist of a large number of grains aggregated, where the grains are bounded microcrystals composed of a large number of crystals. By XRD tests, the grain size of nanomaterials (adapted to the range 1–100 nm) can be calculated using the diffraction peak half-height width based on the Scheele formula, which is as follows:

$$D = K\lambda/(\beta \cos \theta) \tag{2}$$

where D is the grain size, *i.e.*, the diameter of a spherical grain, K is a constant, and λ is the X-ray wavelength. The wavelength of Cu Kα rays is 0.15406 nm, β is the half-height width of the diffraction peak, and θ is diffraction angle corresponding to the diffraction peak. The average grain size of the prepared $NiCo_2O_4$ nanoparticles was calculated to be 13.3 nm using the half-height width of the diffraction peaks mentioned previously. In summary, $NiCo_2O_4$ nanoparticles with a single crystalline phase and small grains were successfully prepared by the hydrothermal method.

The surface morphology of $NiCo_2O_4$ nanoparticles was analysed by scanning electron microscopy. Fig. 1(b) shows the
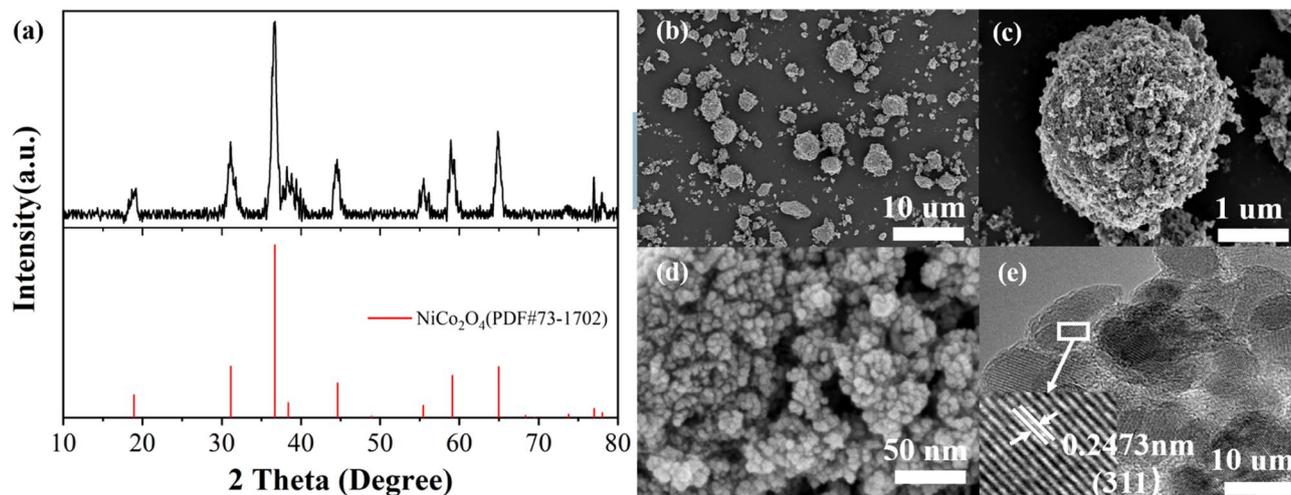
Fig. 1 (a) XRD patterns of NiCo$_2$O$_4$ (b)−(d) SEM image at 10 μm, 1 μm, 50 nm, respectively (e) HRTEM image.

material morphology at a scale of 10 μm. It can be seen that the NiCo$_2$O$_4$ synthesized by hydrothermal method mainly presents spherical granular agglomerates with poor homogeneity and very wide particle size distribution, with larger agglomerates of 7–8 μm in diameter and nanoscale agglomerates showing light spots. Fig. 1(c) shows the surface morphology of the agglomerates with a diameter of 7 μm at a scale of 1 μm, and the surface of the agglomerates is very rough. Fig. 1(d) shows a further

enlargement of the surface morphology of the agglomerates at a scale of 50 nm, and the accumulation of small grains in the figure shows that the agglomerates consist of a large number of grains with a diameter of about 10 nm.

The black areas indicate surface gaps that increase the contact area of the electrolyte. Fig. 1(e) show that the typical lattice spacing of 0.2473 nm corresponds to the (3 1 1) crystal plane of the cubic phase NiCo$_2$O$_4$.

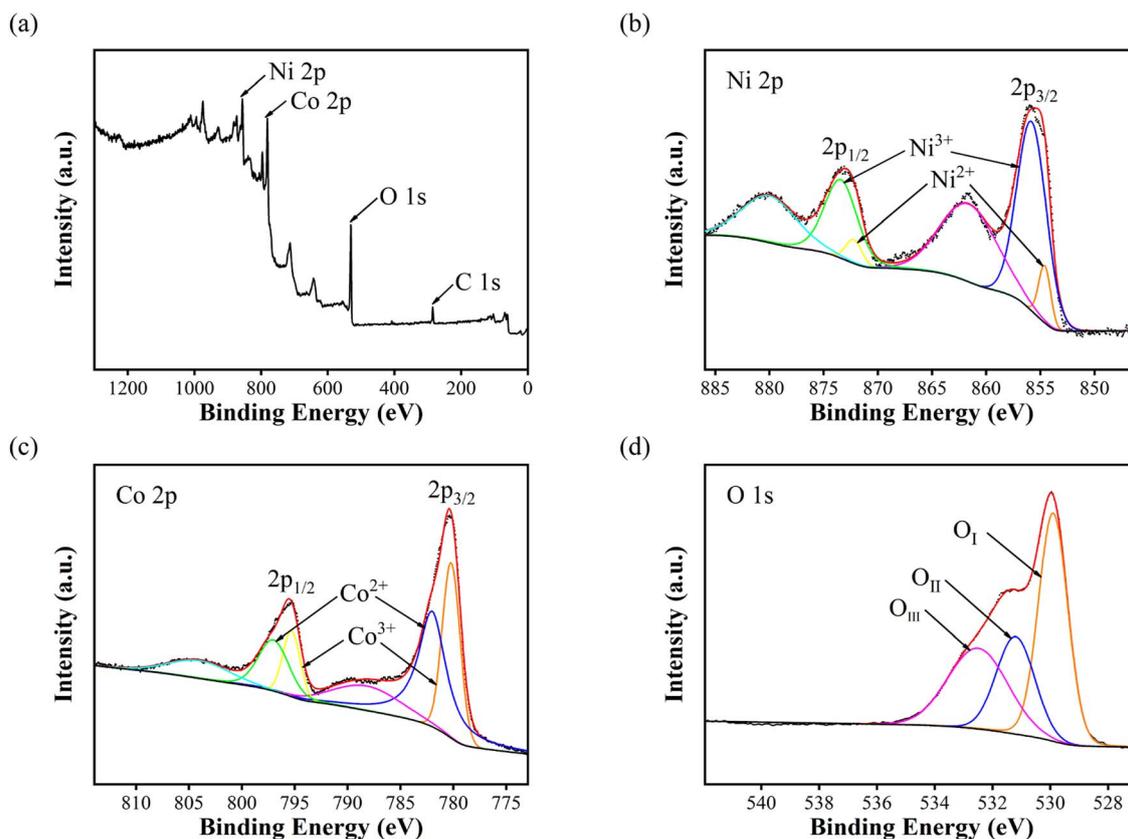Fig. 2 X-ray photoelectron spectra of NiCo$_2$O$_4$ nanoparticles: (a) survey spectrum (b) Ni 2p (c) Co 2p and (d) O 1s.

Table 1 Binding energy and peak area of Ni in $2p_{3/2}$ hybrid orbital

Ni^{2+}		Ni^{3+}		
Binding energy (eV)	Area of peaks (%)	Binding energy (eV)	Area of peaks (%)	Ratio of content Ni^{2+}/Ni^{3+}
854.6	11.0	855.8	89.0	0.12

Table 2 Binding energy and peak area of Co in $2p_{3/2}$ hybrid orbital

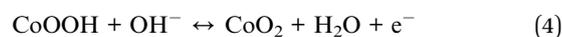| Co^{2+}		Co^{3+}		
Binding energy (eV)	Area of peaks (%)	Binding energy (eV)	Area of peaks (%)	Ratio of content Co^{2+}/Co^{3+}
782.0	60.0	780.2	40.0	1.50

The elemental compositions and valence states of $NiCo_2O_4$ nanoparticles were analysed by X-ray photoelectron spectroscopy. Fig. 2(a) shows the full XPS spectrum of $NiCo_2O_4$ nanoparticles, indicating that only Ni, Co, O and C elements exist in the test sample, and C is the calibration element. Fig. 2(b) shows the Ni 2p spectrum, with two hybrid orbital peaks ($2p_{1/2}$ and $2p_{3/2}$) and two satellite peaks. The peaks of $2p_{1/2}$, $2p_{3/2}$, Ni^{2+} and Ni^{3+} was shown at the Table 1. Fig. 2(c) shows the Co 2p spectrum, which also has two hybrid orbital peaks of $2p_{1/2}$ and $2p_{3/2}$ and two satellite peaks. Table 2 show the peaks of $2p_{1/2}$, $2p_{3/2}$, Co^{2+} and Co^{3+}. Fig. 2(d) shows the O 1s diagram, consisting of O_I, O_{II}, and O_{III}. O_I represents the metal–oxygen bond (O^{2-}) with a peak position of 529.9 eV. O_{II} represents the low coordination oxygen ion (O_2^{2-}/O^-) with a peak of 531.2 eV. O_{III}

represents the oxygen in water or OH^- physically/chemically adsorbed on the material surface, with a peak of 532.5 eV.[15–18]

Under the condition of a certain total amount of elements, the higher the content of +2-valent elements, the higher the content of oxygen vacancy, the more reactive sites, and the stronger the charge storage ability.[19] According to Fig. 2 and Tables 1, 2, since the Ni/Co value in $NiCo_2O_4$ is 0.5, the total ratio of +2-valent elements to +3-valent elements is 0.78, which is higher than the theoretical ratio of 0.5 for spinel structure +2-valent elements to +3-valent elements. The prepared $NiCo_2O_4$ nanoparticles have higher content of +2-valent elements than intact crystals, and may have more active sites.

3.2 Electrochemical characterizations

The behaviour of supercapacitor during charging and discharging of $NiCo_2O_4$ electrode was analyzed by cyclic voltammetry. Fig. 3(a) show the cyclic voltammetry curve of $NiCo_2O_4$ electrode at scanning rate of 10–50 mV s^{-1} under potential window of 0–0.55 V. It can be seen that the curve has an obvious redox peak, indicating the energy storage characteristics of the pseudocapacitor of $NiCo_2O_4$ electrode material. The redox reaction equation is as follows:[20,21]

$$NiCo_2O_4 + OH^- + H_2O \leftrightarrow NiOOH + 2CoOOH + e^- \quad (3)$$

$$CoOOH + OH^- \leftrightarrow CoO_2 + H_2O + e^- \quad (4)$$

There is only one pair of redox peaks in the curve. It is considered that the redox reaction potential of Ni and Co in the charging and discharging process is roughly equal, so the total reaction formula is as follows:
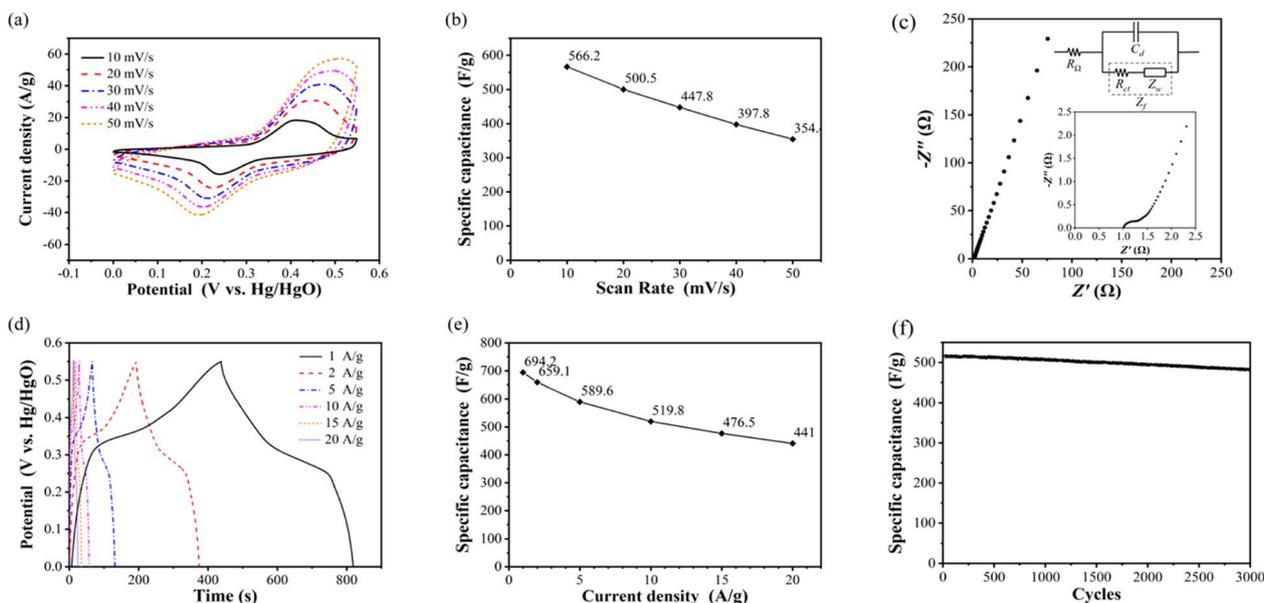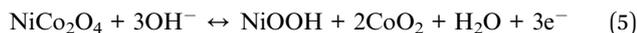

Fig. 3 (a) CV curves of $NiCo_2O_4$ (b) average charge–discharge capacitance (c) electrochemical impedance spectroscopy of $NiCo_2O_4$ (d) GCD curves of $NiCo_2O_4$ (e) discharge specific capacitance (f) cyclic stability curve of $NiCo_2O_4$ electrode.

$$NiCo_2O_4 + 3OH^- \leftrightarrow NiOOH + 2CoO_2 + H_2O + 3e^- \quad (5)$$

At the scanning rate of 10 mV s^{-1}, the oxidation peak and reduction peak are 0.412 V and 0.241 V, respectively. The current density of oxidation peak is 16.1 A g^{-1}, and that of reduction peak is 9.5 A g^{-1}. With the increase of scanning rate, the oxidation peaks potential increases, the reduction peak potential decreases, and the peak current density also increases. When the scanning rate increases to 50 mV s^{-1}, the oxidation peak and reduction peak are located at 0.512 V and 0.193 V, respectively. The current density of oxidation peak is 41.2 A g^{-1}, and that of reduction peak is 15.1 A g^{-1}.

According to the calculation, the specific capacitance of NiCo$_2$O$_4$ electrode at the scanning rate of 10, 20, 30, 40 and 50 mV s^{-1} is 566.2, 500.5, 447.8, 397.8 and 354.4 F g^{-1}, respectively, as shown in Fig. 3(b). With the increase of the scanning rate, the specific capacitance of the electrode decreases, which indicates that the electrode material of the supercapacitor exhibits the multiplier performance similar to that of the battery, that is, with the increase of the charging and discharging current, the amount of electricity that can be stored and discharged decreases.

Fig. 3(c) shows the impedance spectrum of NiCo$_2$O$_4$ electrode measured by sinusoidal AC voltage signal with amplitude of 5 mV in the frequency range of 10^{-2} to 10^5. The intersection of the impedance spectrum with the real axis (horizontal axis) is the internal resistance value, which is 1.0 Ω. It can be seen from the full-frequency impedance spectrum that the internal resistance and charge transfer resistance of NiCo$_2$O$_4$ electrode are very small, and the impedance is mainly determined by the Warburg impedance in the process of material transfer.[22,23]

The specific capacitance and rate performance of NiCo$_2$O$_4$ electrode were analysed by constant current charge–discharge test. Fig. 3(d) shows the constant current charge–discharge curves of NiCo$_2$O$_4$ electrode measured at 1, 2, 5, 10, 15, 20 A g^{-1} at the potential window of 0–0.55 V. The curve of charging process is observed to rise rapidly at first, then slowly, and then quickly again. The curve of discharge process is the shape of rapid decline, then slow decline, and then rapid decline again. This is because the charging and discharging process of NiCo$_2$O$_4$ electrode is controlled by two kinds of energy storage principles: double layer capacitor and pseudocapacitor. With the increase of current density, both the electrostatic adsorption and desorption rate of the double electric layer and the redox reaction rate of the pseudocapacitor increase, and the duration of the rapid and slow change stages of the potential decreases simultaneously, as well as the charge–discharge time. Fig. 3(e) shows the discharge specific capacitance of NiCo$_2$O$_4$ electrode calculated according to eqn (6) at the current density of 1, 2, 5, 10, 15 and 20 A g^{-1}, which are 694.2, 659.1, 589.6, 519.8, 476.5 and 441.0 F g^{-1} respectively. The curve reflects the magnification performance of NiCo$_2$O$_4$ electrode. When the current density increases from 1 A g^{-1} to 20 A g^{-1}, the retention rate of specific capacitance reaches 63.5%, and the decline trend of specific capacitance slows down with the increase of current density. Compared to porous spherical nanostructures

NiCo$_2$O$_4$,[24] the prepared NiCo$_2$O$_4$ nanoparticles have better specific capacitance and rate performance.

$$C_m = \frac{i_m \Delta t}{\Delta V} = \frac{i_m}{dV/dt} \quad (6)$$

where C_m is the specific capacitance value, i_m is the current density, ΔV is the potential change, Δt is the corresponding time, dV/dt is the potential change rate. The charge–discharge capacitance and charge–discharge capacitance can be calculated by the constant current charge–discharge curve. Generally, the charge–discharge capacitance is used as the performance evaluation index.

Cyclic stability is tested through thousands of constant current charge–discharge processes, Fig. 3(f) shows the cyclic stability curve of NiCo$_2$O$_4$ electrode measured at a potential window of 0–0.55 V and a current density of 10 A g^{-1} for 3000 cycles of charging and discharging. It can be seen that the specific capacitance of NiCo$_2$O$_4$ electrode remained basically unchanged in the first 250 cycles, and began to decline slowly after 250 cycles. After 3000 cycles, the specific capacitance decreased from the initial 519.2 F g^{-1} to 481.7 F g^{-1}, and the retention rate of specific capacitance was 92.8%. It is shown that NiCo$_2$O$_4$ electrode has better cyclic stability than sea urchin NiCo$_2$O$_4$ microsphere (capacitance retention rate 81.6% after 5000 cycles at current density 5 A g^{-1}).[25] The strong crystal structure of NiCo$_2$O$_4$ makes it resistant to material structure damage, so it shows excellent cyclic stability and has practical application potential.

NiCo$_2$O$_4$ cathode electrode and GO anode electrode are prepared to make NiCo$_2$O$_4$//GO asymmetric supercapacitor, which can be charged and discharged for 3000 times at the current density of 10 A g^{-1}. The electrochemical performance of NiCo$_2$O$_4$//GO asymmetric supercapacitor was tested by cyclic voltammetry test and constant current charge–discharge test, and the decay process was analysed by comparing the performance with that before cyclic.

Fig. 4(a) shows the comparison of cyclic voltammetry curves of NiCo$_2$O$_4$//GO asymmetric supercapacitor with scanning rates of 10, 30 and 50 mV s^{-1} at the voltage range of 0–1.7 V before and after 3000 cycles. It can be seen that the charge–discharge current density of NiCo$_2$O$_4$//GO asymmetric supercapacitor decreases after cycling, and the charging current density after cycling changes little compared with that before cycling. It only decreases when it is higher than the oxidation peak potential and approaches the upper cut off potential, and shows the weakening of polarization phenomenon.

Fig. 4(b) shows the comparison of constant current charge and discharge curves of NiCo$_2$O$_4$//GO asymmetric supercapacitor with current density of 1 and 10 A g^{-1} in the voltage range of 0–1.7 V before and after cycling. It can be seen that the charge–discharge time after the cycle decreases, indicating that the specific capacitance decreases. In general, the specific capacitance retention rate is used to represent the cycle stability, and the specific capacitance loss is also an important method to represent the cycle decline.

Fig. 4(c) shows that the specific capacitance of the asymmetric supercapacitor before and after the cycle decreases to
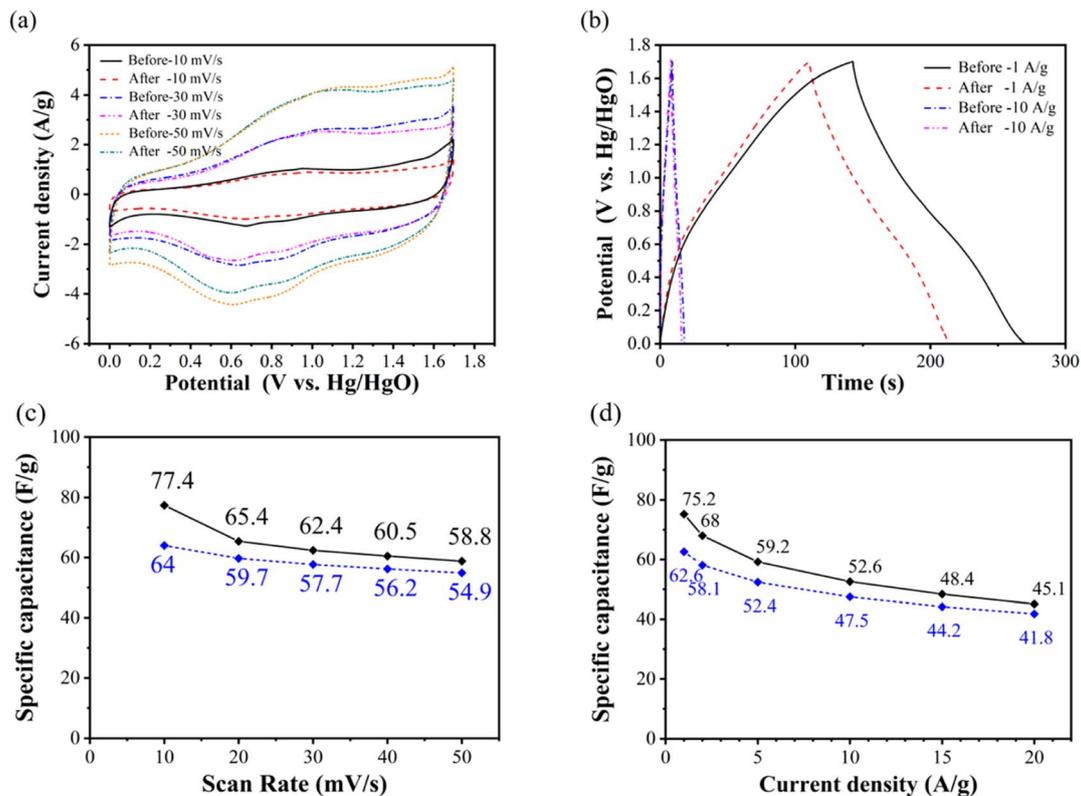
Fig. 4 Comparison of electrochemical performance test results of NiCo$_2$O$_4$//GO asymmetric supercapacitor before and after cyclic test: (a) CV curves (b) GCD curves (c) average charge–discharge capacitance (d) discharge specific capacitance.

a certain extent at different scanning rates. Moreover, Fig. 4(d) shows the specific discharge capacitance of NiCo$_2$O$_4$//GO asymmetric supercapacitor calculated according to eqn (6) at the current density of 1, 2, 5, 10, 15 and 20 A g^{-1} before and after 3000 cycles. It can be seen that the specific capacitance decreases overall after cycling, but the multiplier performance improves instead. Before the cycle, when the current density increases from 1 A g^{-1} to 20 A g^{-1}, the specific capacitance retention rate is 60.0%. After cycling, the specific capacitance retention rate is increased to 66.8%. This is because after 3000 cycles at 10 A g^{-1} current density, NiCo$_2$O$_4$//GO asymmetric supercapacitors exhibit greater specific capacitance loss at low current density than at high current density. Supercapacitor at 1 A g^{-1} current density, the specific capacitance loss is 16.8%, and at the current density of 20 A g^{-1}, the specific capacitance loss is only 7.3%.

3.3 Study on the mechanism of electrode decay

After cycling, the discharge specific capacitance of NiCo$_2$O$_4$ electrode decreases, which is one of the main reasons for the performance decline of NiCo$_2$O$_4$//GO asymmetric supercapacitor. By ultrasonic oscillation, the binder polyvinylidene fluoride was quickly dissolved in 1-methyl-2-pyrrodanone to make the electrode active material fall off from the electrode sheet, and the recycled NiCo$_2$O$_4$ material was characterized by its surface morphology, crystal structure and elemental composition.

The morphology of NiCo$_2$O$_4$ was analysed by scanning electron microscope. Fig. 5(a) and (d) show the material morphology at a scale of 10 μm before and after cycling, respectively. After cycling, the shape of aggregates becomes irregular compared with that before cycling, and the number of small particles increases significantly. Fig. 5(b) and (e) show the surface morphologies of aggregates at 100 nm before and after cycling, respectively; (c) and (f) show the surface morphologies of aggregates at 50 nm before and after cycling, respectively. The comparison of the surface morphology of aggregates before and after the cycle shows that the aggregates still have rough and slotted surface morphology, but the porosity increases. The proportion of pore area in Fig. 5(b) and (e) calculated on basis of gray scale increases from about 7.3% to 16.6%. The increase of porosity will reduce the charge transfer resistance, realize the rapid electron transfer of the electrode and reduce the volume change during the charge–discharge cycle, thus having a positive impact on the electrochemical performance and stability of the electrode materials.[26,27]

Through X-ray diffraction analysis, the crystal phase composition and crystal structure of NiCo$_2$O$_4$ material recovered from the recycled cathode electrode were analysed, and the results are shown in Fig. 6(a). The XRD pattern of the recycled material is no longer a single NiCo$_2$O$_4$ crystal phase, but a hybrid peak of multiple crystal phases superposition, such as CoOOH, CoO, CoC$_2$O$_4$·2H$_2$O, NiC$_4$H$_4$O$_6$·2.5H$_2$O, appears at 2θ values of about 22°, 29°, 33°, 42°, 47°, 53°, 63° and 74°. The
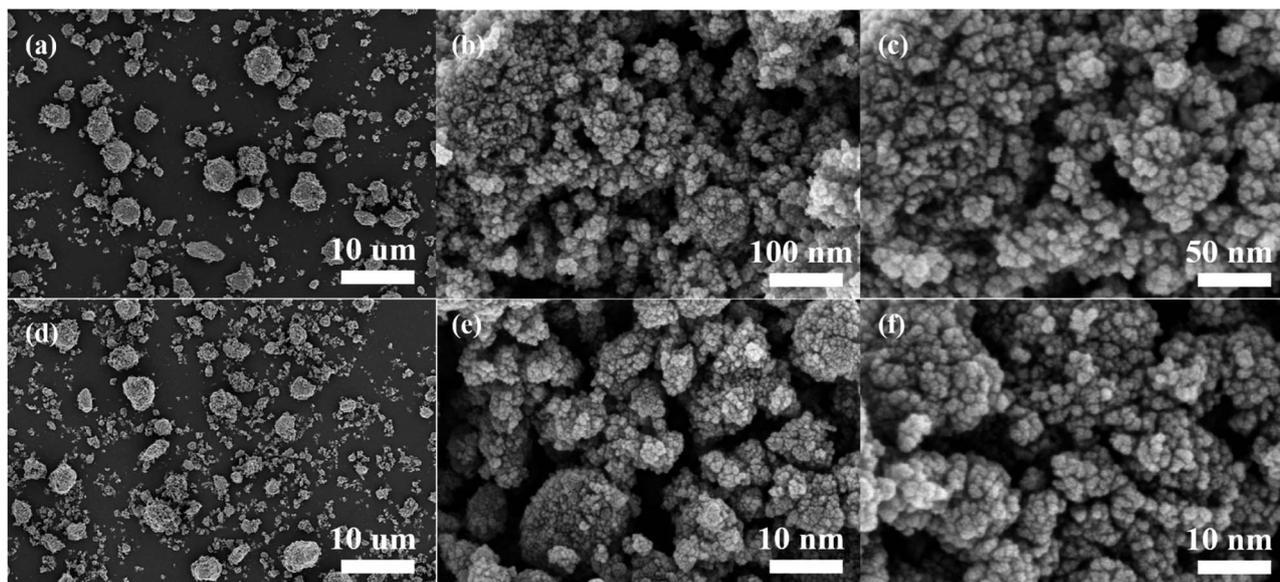
Fig. 5 Comparison of scanning electron microscopy images before and after cyclic testing of cathode active material: (a)–(c) are before the cycle; (d)–(f) are after the cycle.
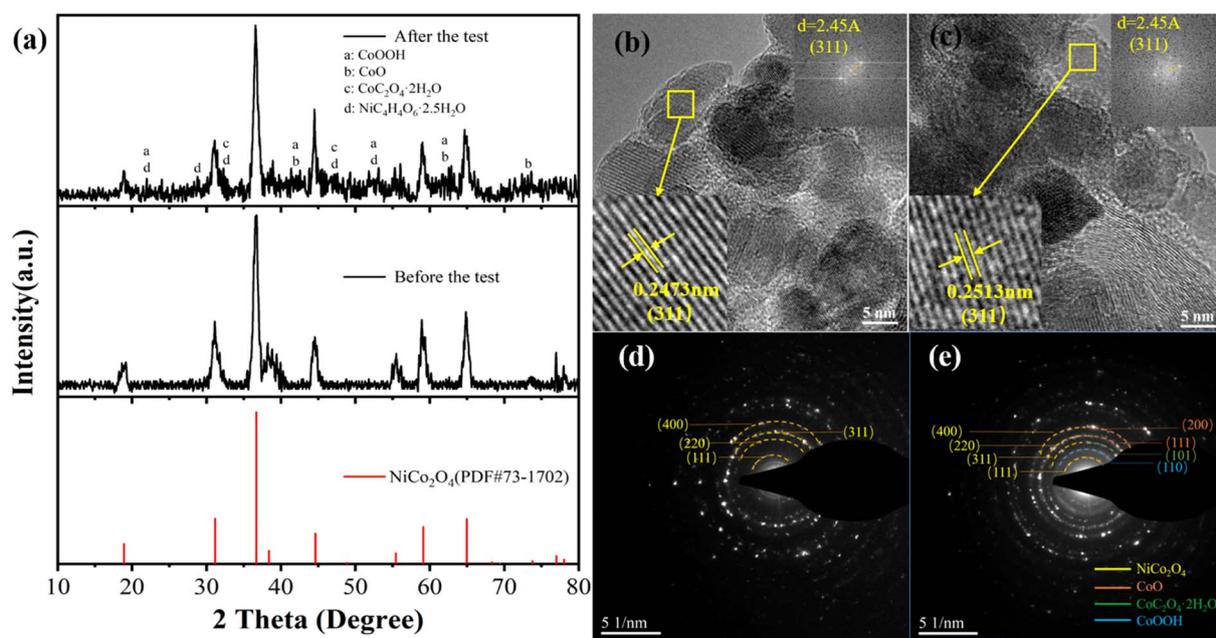

Fig. 6 (a) XRD image before and after cyclic testing of $NiCo_2O_4$ electrode (b) HRTEM image before the cycle (c) HRTEM image after the cycle (d) SAED pattern of $NiCo_2O_4$ before the test (e) SAED pattern of $NiCo_2O_4$ after the test.

results show that the structure of $NiCo_2O_4$ is damaged and mixed with various crystals during the electrochemical cycle. The average grain size of $NiCo_2O_4$ after the cycle is 11.4 nm by using the half-height and width of the diffraction peak, which decreases compared with 13.3 nm before the cycle, which also indicates the failure of the crystal structure of $NiCo_2O_4$. The destruction of crystal structure and the disorder of crystal phase indicate the material destruction of $NiCo_2O_4$ nanoparticles during the electrochemical cycle. Fig. 6(b) and (c) compared

HRTEM images before and after the cycle, which found that for the same crystal plane (311), the lattice spacing changes from 0.2473 nm to 0.2513 nm. As the crystal plane spacing becomes larger, the structural period of the crystal will also become larger, resulting in the deterioration of crystal stability. The increase of lattice spacing causes the 2θ value of the characteristic peak (311) in the XRD pattern to shift from 36.7° to 36.6°, which changes the crystal structure and ultimately leads to the degradation of the performance of $NiCo_2O_4$ electrode.[28]

Selected-area electron diffraction (SAED) was conducted to estimate the crystallinity of NiCo$_2$O$_4$, which is shown in the inset of Fig. 6(d). The diffraction rings can be indexed to the (111), (220), (311) and (400) planes of cubic NiCo$_2$O$_4$ as marked in Fig. 6(a), respectively, indicating the poly-crystalline structure of NiCo$_2$O$_4$. Fig. 6(e) is the diffraction ring pattern after the cycle. Compared with Fig. 6(d), it is found that many impurities are produced, in which the characteristic crystal plane shown by the generation of impurity can correspond to the impurities produced in the XRD pattern. Orange represents the impurity CoO two characteristic crystal planes are (200), (111) respectively. Green is the (101) characteristic crystal plane of CoC$_2$O$_4$·2H$_2$O; blue is the newly added diffraction ring corresponding to the (110) crystal plane of CoOOH.

Fig. 7 shows the HRTEM diagram after cycling. It can be seen in Fig. 7(a) that a new lattice spacing of 0.1984 nm appears after

cycling, corresponding to the (220) characteristic crystal face of the newly formed impurity CoC$_2$O$_4$·2H$_2$O. Orange corresponds to the CoOOH characteristic crystal face whose crystal spacing is 0.2116 nm. In Fig. 7(b), it can be seen that the two characteristic crystal faces of the impurity CoOOH (111) and (110) correspond to lattice spacing of 0.2318 and 0.3960 nm, respectively. These HRTEM diagrams confirm the above analysis combined with XRD and SAED diagrams, proving the formation of the above-mentioned impurities. The comparative analysis further confirmed the formation of various impurities after circulation. The above analysis of the crystal structure shows that the crystal structure of the electrode has been destroyed after the cyclic test, leading to the deterioration of the performance.

The elemental valence of NiCo$_2$O$_4$ was analysed by XPS, and the ratio of the content of +2-valent element and +3-valent element was calculated. The change of elemental valence in
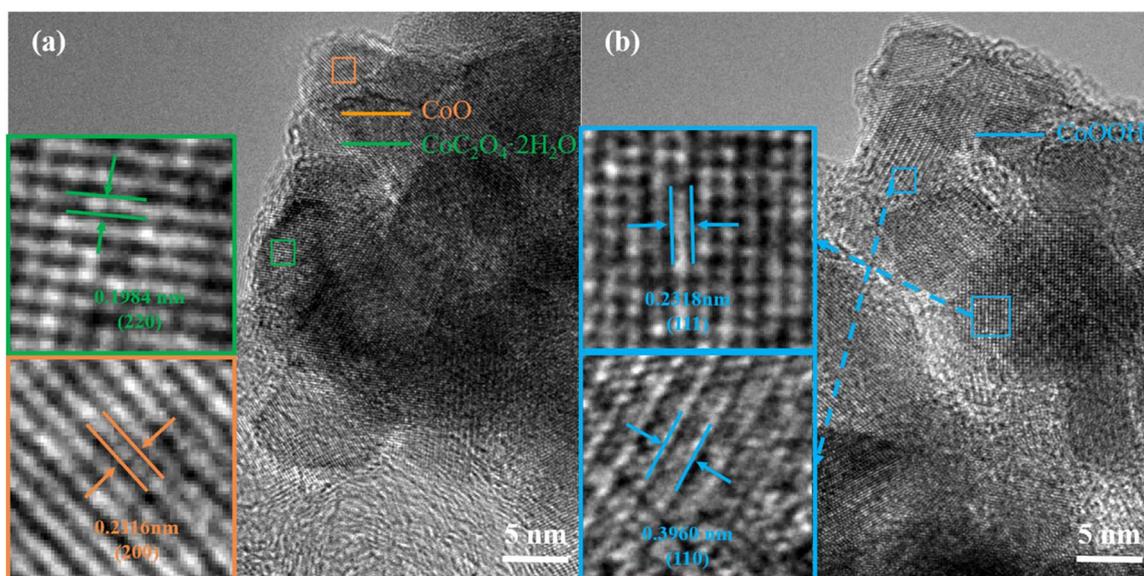

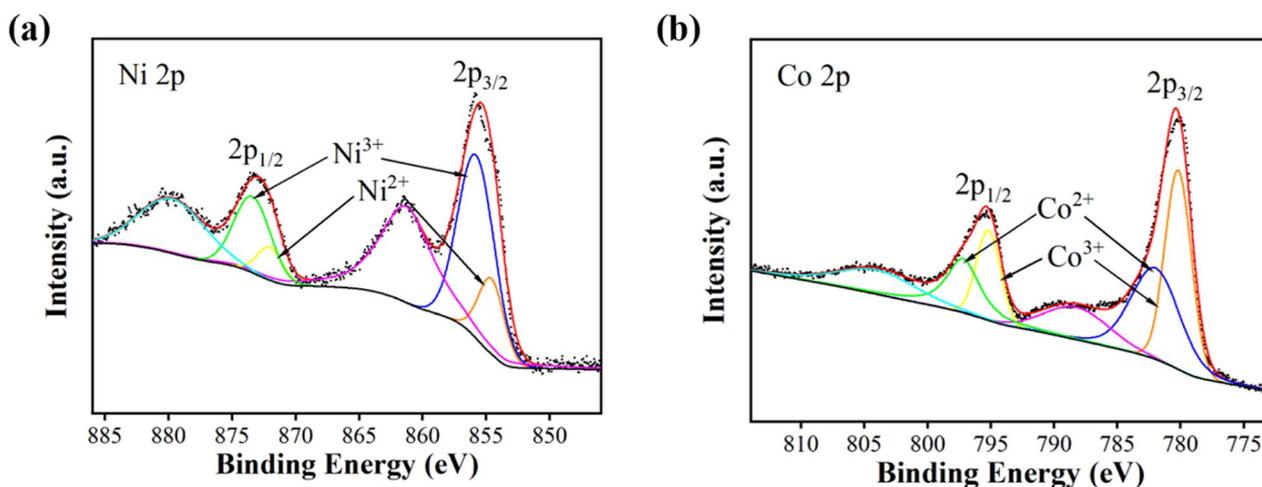Fig. 7 (a) and (b) are different HRTEM image after the cycle.

Fig. 8 X-ray patterns after cyclic testing of cathode active materials: (a) Ni 2p (b) Co 2p.

$NiCo_2O_4$ after cyclic decay was studied. Fig. 8 shows the comparison of XPS spectra after the cycle. (a) and (b) are Ni 2p spectrum and Co 2p spectrum after the cycle, respectively. After the cycle, the peaks of $2p_{1/2}$ and $2p_{3/2}$ of the Ni 2p spectrum remain around 873.1 eV and 855.8 eV, and the peak-to-peak of the Ni 2p spectrum also remain unchanged. The $2p_{1/2}$ and $2p_{3/2}$ peaks of the Co 2p spectrum are about 795.0 eV and 780.0 eV, which slightly decrease compared with before the cycle, but the peak-to-peak remains unchanged. The XPS atlas was used to calculate the peak area of Ni and Co in the $2p_{3/2}$ hybrid orbital and the ratio of the two valence elements in the cycled $NiCo_2O_4$. The results are shown in Tables 3 and 4. The value of Ni^{2+}/Ni^{3+} is 0.29, and the value of Co^{2+}/Co^{3+} is 0.92. After cycling, the content of Ni^{2+} in Ni increases, while the content of Co^{2+} in Co decreases, indicating that Ni in $NiCo_2O_4$ is more inclined to reduction, while Co is more inclined to oxidation during the electrochemical cycling process. The total ratio of +2-valent element to +3-valent element is reduced to 0.65, indicating that the redox reaction of $NiCo_2O_4$ is not completely reversible, and the active sites are reduced, leading to the deterioration of properties.

Fig. 9(a) EIS comparison of $NiCo_2O_4$ electrode before and after cycling. According to the figure, the R_Ω value after cycling decreases from 1.0 Ω to 0.9 Ω, and the R_{ct} value from 0.3 Ω to 0.1 Ω, and the impedance mode is also greatly reduced, but the electrochemical impedance of $NiCo_2O_4$ electrode decreases after cycling. After cycling, the specific capacitance of $NiCo_2O_4$ electrode is mainly affected by the crystal phase change of $NiCo_2O_4$ material, the destruction of crystal structure and the reduction of active site, and the performance declines, while the power performance is little affected by the change of $NiCo_2O_4$ material. The electrochemical impedance of $NiCo_2O_4$ is more affected by the dispersion of $NiCo_2O_4$ aggregates and the increase of porosity.

The charge storage capacity reflected by the specific capacitance is the most important electrochemical performance of the electrode, so it is considered that the electrochemical performance of the electrode deteriorates overall after cycling. The current density will affect the cyclic stability of $NiCo_2O_4$//GO asymmetric supercapacitor. Fig. 9(b) shows the cycle stability curve of $NiCo_2O_4$//GO asymmetric supercapacitor measured by 5, 10, 15 and 20 A g^{-1} cycles of charge and discharge 3000 times

Table 3 Binding energy and peak area of Ni in $2p_{3/2}$ hybrid orbital

	Ni^{2+}		Ni^{3+}		Ratio of content Ni^{2+}/Ni^{3+}
	Binding energy (eV)	Area of peaks (%)	Binding energy (eV)	Area of peaks (%)	
Before	854.6	11.0	855.8	89.0	0.12
After	854.6	22.6	855.8	77.4	0.29

Table 4 Binding energy and peak area of Co in $2p_{3/2}$ hybrid orbital

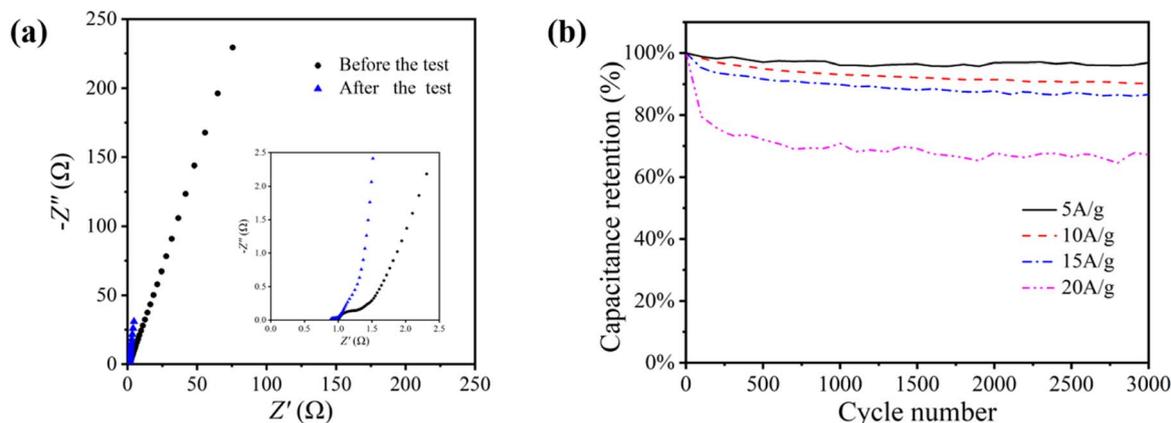|	Co^{2+}		Co^{3+}		Ratio of content Co^{2+}/Co^{3+}
	Binding energy (eV)	Area of peaks (%)	Binding energy (eV)	Area of peaks (%)	
Before	782.0	60.0	780.2	40.0	1.50
After	782.0	48.0	780.2	52.0	0.92

Fig. 9 (a) EIS comparison curves before and after the cycle (b) cyclic stability curve comparison of $NiCo_2O_4$//GO asymmetric supercapacitor.

at the voltage range of 0–1.7 V. The specific capacitance of NiCo$_2$O$_4$//GO asymmetric supercapacitor drops rapidly in the first few hundred cycles, and then the curve flattens out. During the cycle, material destruction and the reduction of active sites lead to the performance decline, while the increase of porosity slows down the performance decline to some extent. With the increase of current density, the cyclic decay of NiCo$_2$O$_4$//GO asymmetric supercapacitor is intensified, and the cyclic decay is extremely fast at the high current density of 20 A g^{-1}.

In order to improve the cycle stability of the electrode material, the first is to make NiCo$_2$O$_4$ nanoparticles grow directly on the collector, which can improve its electrochemical performance and cycle stability. The traditional polyvinylidene fluoride (PVDF) binder is easy to absorb the electrolyte and swell, resulting in a decline in the bonding performance, thus making its electrochemical performance decline. Second, the surface morphology of the fluid collector can be changed. The larger the surface roughness of the fluid collector, the larger the conductive contact area between the active substance and the fluid collector, the higher the adhesion strength, and the more difficult it is to peel off during the charging and discharging process, thus having higher cyclic stability. Third, it is necessary to ensure that the electrode material reduces contact with the air during work to prevent oxidation into other impurities during work, resulting in changes in the composition and crystal structure of NiCo$_2$O$_4$; besides, reducing the electrode load during operation and reducing the current density of the electrode material can greatly improve its cycle stability.[29–31]

4. Conclusions

In order to study the degradation mechanism of NiCo$_2$O$_4$//GO asymmetric supercapacitors, NiCo$_2$O$_4$ nanoparticles were prepared by hydrothermal method with a single phase and a smaller grain size of 13.3 nm. The aggregate particle size of the material is widely distributed and the surface morphology is rough and interstitial. NiCo$_2$O$_4$ electrode was prepared by coating method using NiCo$_2$O$_4$ as electrode active material. NiCo$_2$O$_4$//GO asymmetric supercapacitor was constructed and tested for 3000 times of charging and discharging at a current density of 10 A g^{-1}. The cyclic decay of the NiCo$_2$O$_4$ electrode before and after the cycle is analysed. The cyclic decay of the asymmetric supercapacitor is mainly caused by the decay of the pseudocapacitance of the active material of the NiCo$_2$O$_4$ electrode, and is also affected by other factors such as the decay of electrolyte and fluid collector. The following conclusions were reached:

By comparing XRD patterns before and after the cycle, it can be seen that there are heterogeneous peaks of multiple crystal phases superposition, such as CoOOH, CoO, CoC$_2$O$_4$·2H$_2$O, NiC$_4$H$_4$O$_6$·2.5H$_2$O, etc., which indicates that the structure of NiCo$_2$O$_4$ is damaged and a variety of crystal phases are mixed during the electrochemical cycle. This leads to the degradation of electrode performance. After the cycle, the aggregate particles of NiCo$_2$O$_4$ materials are more dispersed and the porosity increases, but the surface morphology is still rough. According to the analysis of the HETEM and SAED diagrams, the lattice

spacing of the crystal structure increases before and after the cycle, and the crystal structure is in disorder due to the generation of new substances. Compared with the previous damage, the stability of the electrode has been reduced and the performance of the pseudocapacitor has been decreased. This is one of the main reasons leading to the performance decline of asymmetric supercapacitors. The results of X-ray photoelectron spectroscopy showed that the relative content of Ni^{2+} in Ni increased, the relative content of Co^{3+} in Co increased, and the total ratio of +2-valent element to +3-valent element decreased from 0.78 to 0.65, and the active site decreased. The change of crystal phase, the increase of lattice spacing leading to the destruction of crystal structure and the decrease of active sites are the main reasons for the degradation of electrochemical performance of NiCo$_2$O$_4$ electrode represented by specific capacitance, while the agglomeration particles are more dispersed, and the increase of porosity has a positive effect on slowing down the degradation. Therefore, when the electrode is used, it is necessary to minimize the contact with the air and control it to work at the most appropriate current density in order to delay the degradation of the electrode material. It has a good reference significance for improving the cycle stability of electrode materials.

Conflicts of interest

None.

Acknowledgements

References

1 Z. Lin, E. Goikolea, A. Balducci, *et al.*, Materials for supercapacitors: when Li-ion battery power is not enough, *Mater. Today*, 2018, **21**(4), 419–436.

2 B. E. Conway, *Electrochemical Supercapacitors: Scientific, Fundamentals, and Technological Applications*, Kluwer Academic/Pemum Publishers, New York, 1999.

3 Y. Shao, M. El-Kady, J. Sun, *et al.*, Design and Mechanisms of Asymmetric Supercapacitors (Review), *Chem. Rev.*, 2018, **118**(18), 9233–9280.

4 Q. Zhang and G. Li, Experimental Study on a Semi-active Battery-Supercapacitor Hybrid Energy Storage System for Electric Vehicle Application, *IEEE Trans. Power Electron.*, 2020, **35**(1), 1014–1021.

5 Z. Song, J. Li, J. Hou, *et al.*, The battery-supercapacitor hybrid energy storage system in electric vehicle applications: a case study, *Energy*, 2018, **145**(1), 433–441.

6 X. Ni, K. Li, C. Li, *et al.*, Construction of NiCo$_2$O$_4$ nanoflake arrays on cellulose-derived carbon nanofibers as a freestanding electrode for high-performance supercapacitors, *Front. Chem. Sci. Eng.*, 2023, **17**(6), 691–703.

7 F. Li, Q. Li, H. Kimura, *et al.*, Morphology controllable urchin-shaped bimetallic nickel-cobalt oxide/carbon composites with enhanced electromagnetic wave

absorption performance, *J. Mater. Sci. Technol.*, 2023, **148**(17), 250–259.

8 M. A. Yewale, R. A. Kadam, N. K. Kaushik, *et al.*, Interconnected plate-like $NiCo_2O_4$ microstructures for supercapacitor application, *Mater. Sci. Eng., B*, 2023, 287.

9 L. Pio Di Noia, F. Genduso, R. Miceli, *et al.*, Optimal Integration of Hybrid Supercapacitor and IPT System for a Free-Catenary Tramway, *IEEE Trans. Ind. Appl.*, 2019, **55**(1), 794–801.

10 C. Julien and A. Mauger, Nanostructured MnO_2 as electrode materials for energy storage (review), *Nanomaterials*, 2017, **7**(11), 396.

11 T. Liu, Y. Li, *et al.*, Addressing the Achilles' heel of pseudocapacitive materials: long-term stability, *InfoMat*, 2020, **2**(5), 807–842.

12 S. Liu, L. Wei, H. Wang, *et al.*, Review on reliability of supercapacitors in energy storage applications, *Applied Energy*, 2020, **278**, 115436.

13 Y. Sun, J. Zhang, X. Sun, *et al.*, High-performance spinel $NiMn_2O_4$ microspheres self-assembled with nanosheets by microwave-assisted synthesis for supercapacitors, *CrystEngComm*, 2020, **22**(9), 1645–1652.

14 F. Bao, X. Wang, X. Zhao, *et al.*, Controlled growth of mesoporous $ZnCo_2O_4$ nanosheet arrays on Ni foam as high-rate electrodes for supercapacitors, *RSC Adv.*, 2014, **4**, 2393–2397.

15 T. Liu, S. Zhou, X. Yu, C. Mao, Y. Wei, X. Yu, L. Chen, X. Zhao, G. Tian and L. Chen, *RSC Adv.*, 2022, **12**, 4029–4041.

16 L. Miao, Z. Song, W. Du, X. Zheng, Y. Lv, L. Gan and M. Liu, Advances in organic cathode materials for aqueous multivalent metal-ion storage, *Mater. Chem. Front.*, 2023, **7**, 2731–2749.

17 J. Wei, *Study on nickel cobalt oxide nanostructure and supercapacitor performance*, Shenyang University of Technology, Shenyang, 2019.

18 Z. Weiqian, *Study on preparation and electrochemical application of nickel cobalate materials with different morphologies*, Qilu University of Technology, Jinan, 2019.

19 G. Guo, K. Ouyang, J. Yu, *et al.*, Facile Synthesis of $LaCoO_3$ with a High Oxygen Vacancy Concentration by the Plasma Etching Technique for High-Performance Oxygen Ion Intercalation Pseudocapacitors, *ACS Appl. Energy Mater.*, 2019, **3**(1), 300–308.

20 X. Liu, Y. Zhang, X. Xia, *et al.*, Self-assembled porous $NiCo_2O_4$ hetero-structure array for electrochemical capacitor, *J. Power Sources*, 2013, **239**, 157–163.

21 S. Gao, F. Liao, S. Ma, *et al.*, Network-like mesoporous $NiCo_2O_4$ grown on carbon cloth for high-performance pseudocapacitors, *J. Mater. Chem. A*, 2015, **3**(32), 16520–16527.

22 J. Barqi, S. M. Masoudpanah, M. Hasheminiasari, *et al.*, Nanoribbon-like $NiCo_2O_4$/reduced graphene oxide nanocomposite for high-performance hybrid supercapacitor, *J. Alloys Compd.*, 2023, 930.

23 J.-G. Seong, T. H. Ko, D. Lei, *et al.*, Engineered NiCo-LDH nanosheets-and $ZnFe_2O_4$ nanocubes-decorated carbon nanofiber bonded mats for high-rate asymmetric supercapacitors, *Green Energy Environ.*, 2022, **7**(6), 1228–1240.

24 C. Li, Y. Liu, G. Li, *et al.*, Preparation and electrochemical properties of nanostructured porous spherical $NiCo_2O_4$ materials, *RSC Adv.*, 2020, **10**(16), 9438–9443.

25 S. Yan, S. Luo, M. Sun, *et al.*, Facile hydrothermal synthesis of urchin-like $NiCo_2O_4$ as advanced electrochemical pseudocapacitor materials, *Int. J. Energy Res.*, 2021, **45**, 20186–20198.

26 B. Krüner, A. Schreiber, A. Tolosa, *et al.*, Nitrogen-containing novolac-derived carbon beads as electrode material for supercapacitors, *Carbon*, 2018, **132**, 220–231.

27 H. Yang, X. Sun, H. Zhu, *et al.*, Nano-porous carbon materials derived from different biomasses for high performance supercapacitors, *Ceram. Int.*, 2020, **46**, 5811–5820.

28 T. Liu, Y. Li, *et al.*, Addressing the Achilles' heel of pseudocapacitive materials: long-term stability, *InfoMat*, 2020, **2**(5), 807–842.

29 X. Chen, Q. Su, J. Yu, *et al.*, Experimental study on the degradation mechanism of $LaCoO_3$-based symmetric supercapacitors, *RSC Adv.*, 2021, **11**(41), 25170–25178.

30 X. Zheng, L. Miao, Z. Song, *et al.*, *In situ* nanoarchitecturing of conjugated polyamide network-derived carbon cathodes toward high energy-power Zn-ion capacitors, *RSC Adv.*, 2022, **10**(2), 611–621.

31 G. Guanlun and S. Qiwei, Cycling stability of Fe_2O_3 nanosheets as supercapacitor sheet electrodes enhanced by $MgFe_2O_4$ nanoparticles, *RSC Adv.*, 2023, **6**, 3643–3651.